Optics and mechanisms for the Extreme-Ultraviolet Imaging Spectrometer on the Solar-B satellite

Clarence M. Korendyke, Charles M. Brown, Roger J. Thomas, Christian Keyser, Joseph Davila, Robert Hagood, Hirohisa Hara, Klaus Heidemann, Adrian M. James, James Lang, John T. Mariska, John Moser, Robert Moye, Steven Myers, Brian J. Probyn, John F. Seely, John Shea, Ed Shepler, and Jason Tandy

The Extreme-Ultraviolet Imaging Spectrometer (EIS) is the first of a new generation of normal-incidence, two-optical-element spectroscopic instruments developed for space solar extreme-ultraviolet astronomy. The instrument is currently mounted on the Solar-B satellite for a planned launch in late 2006. The instrument observes in two spectral bands, 170–210 Å and 250–290 Å. The spectrograph geometry and grating prescription were optimized to obtain excellent imaging while still maintaining readily achievable physical and fabrication tolerances. A refined technique using low ruling density surrogate gratings and optical metrology was developed to align the instrument with visible light. Slit rasters of the solar surface are obtained by mechanically tilting the mirror. A slit exchange mechanism allows selection among four slits at the telescope focal plane. Each slit is precisely located at the focal plane. The spectrograph imaging performance was optically characterized in the laboratory. The resolution was measured using the Mg III and Ne III lines in the range of 171–200 Å. The He II line at 256 Å and Ne III lines were used in the range of 251–284 Å. The measurements demonstrate an equivalent resolution of ~2 arc sec on the solar surface, in good agreement with the predicted performance. We describe the EIS optics, mechanisms, and measured performance. © 2006 Optical Society of America

OCIS codes: 120.6200, 300.6540, 350.6090, 120.4570, 230.1950.

1. Introduction

The principal objective of the Extreme-Ultraviolet Imaging Spectrometer (EIS) instrument is to obtain spatially and temporally resolved spectroscopic observations[1] of solar structures routinely observed with current large-bandpass extreme-ultraviolet (EUV) and broadband x-ray solar disk imagers. Spectroscopic line profile observations provide direct measurement of line of sight and turbulent bulk flow velocities. The EIS will observe the Sun using spectral lines emitted from a number of ions and ionization states. Ratios of selected sensitive line pairs will directly measure the filling factors of coronal loops to probe for fine-scale structures. Emission lines in the chosen wave bands provide coverage of a range of temperatures present in the solar transition region, coronal, and flare plasmas. The resulting spectroscopic measurements of temperature, density, and velocity are vitally important to progress the increasingly complex and realistic picture of the solar atmosphere emerging from current observations and theory.

An international collaboration of scientists and engineers from the United States, the United Kingdom, and Japan have designed and built the EIS instrument to record high-resolution stigmatic EUV images and spectra of the solar atmosphere.[2] The spectrometer and telescope optics and associated mechanisms were developed for the EIS on the Solar-B satellite

C. M. Korendyke, C. M. Brown (cbrown@ssd5.nrl.navy.mil), C. Keyser, J. T. Mariska, J. Moser, R. Moye, S. Myers, J. F. Seely, and E. Shepler are with the Space Science Division, U.S. Naval Research Laboratory, 4555 Overlook Avenue, S.W., Washington, D.C. 20375. R. J. Thomas and J. Davila are with the Solar Physics Laboratory, NASA Goddard Space Flight Center, Greenbelt, Maryland 20771. R. Hagood is with Swales Aerospace, 5050 Powder Mill Road, Beltsville, Maryland 20705. H. Hara is with the National Astronomical Observatory of Japan, Mitaka, Tokyo 181-8588, Japan. K. Heidemann is with Carl Zeiss Laser Optics, GmbH, D-73447 Oberkochen, Germany. A. M. James and J. Tandy are with the Mullard Space Science Laboratory, University College London, Holmbury Saint Mary, Surrey RH5 6NT, United Kingdom. J. Lang is with the Rutherford Appleton Laboratory, Chilton, Didcot, Oxfordshire OX11 0QX, United Kingdom. B. J. Probyn is with the School of Physics and Space Research, the University of Birmingham, Birmingham B15 2TT, United Kingdom. J. Shea is with the Perdix Corporation, P.O. Box 23, Wilton, New Hampshire 03086.

Received 24 May 2006; accepted 1 August 2006; posted 18 August 2006 (Doc. ID 71325).

0003-6935/06/348674-15$15.00/0

© 2006 Optical Society of America

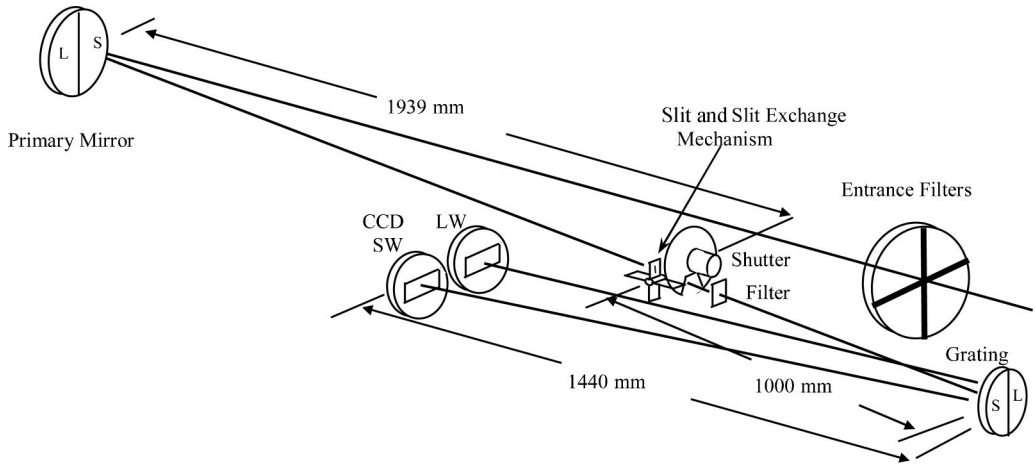

Fig. 1. Schematic layout of the EIS telescope and spectrograph. SW, short wavelength; LW, long wavelength.

by the U.S. Naval Research Laboratory (NRL) (Washington, D.C.) in collaboration with the NASA Goddard Space Flight Center (Greenbelt, Maryland). We present a description of the optics as well as mechanisms as well as their measured performance.

2. Optical Design and Mechanical Elements

A. Optical Design

A number of telescope and spectrometer configurations[3–5] were studied in the planning of this instrument. These included two-mirror Cassegrain-type telescopes and various aberration-corrected grating spectrometers. In the end, a single-mirror off-axis parabola was chosen for the telescope to minimize the number of reflections. For the spectrometer, a toroidal grating with constant groove spacing was chosen, both for its simplicity of manufacture and for its imaging performance. The resulting instrument requires only two reflections, giving a simple reliable instrument with higher throughput than those with more reflections.

An optical schematic of the EIS is shown in Fig. 1. The telescope mirror images EUV radiation from the Sun onto the spectrograph slit. Light passing through the slit is dispersed and stigmatically reimaged by the toroidal grating onto two 1024 pixel × 2048 pixel CCD detectors. The focus of the grating can be remotely adjusted with a mechanism. In flight, the mirror will be rotated in ~0.125 arc sec increments about the Y axis [solar north–south (N-S)] to sample different structures of the solar surface with the slit. High-resolution spectroheliograms (raster images) are formed by steadily moving the solar image in fine increments on the spectrograph slit and taking repeated exposures. An interchange mechanism allows selection among two slits (1 and 2 arc sec wide) and two slots (40 or 266 arc sec wide). The slot observations of the solar disk produce spectrally pure images of large areas of the disk in bright solar emission lines with each exposure. The slot images exhibit a modest spatial blur along the dispersion direction.

Both the mirror and the grating operate at near normal incidence and are coated with Mo/Si multilayer coatings. To broaden the spectral range, the optical elements were divided into two D-shaped sectors; each sector was coated with a multilayer tuned to pro-

Table 1. EIS Toroidal Grating Figure Summary

Grating Number	Used as	Radius 1 (mm)	Radius 2 (mm)	Average Radius (mm)	Slope Error (arc sec)	Radius 1/ Radius 2	Deviation from Specification	Deviation from Mean Value
0	Flight spare	1178.135	1182.740	1180.438	0.45	1.00391	−0.00005	−0.00009
1	Flight spare	1178.176	1182.785	1180.481	0.48	1.00391	−0.00004	−0.00008
2	Flight spare	1178.130	1182.890	1180.510	0.40	1.00404	0.00009	0.00005
3	Alignment	1178.100	1182.886	1180.493	0.40	1.00406	0.00011	0.00007
4	Alignment	1178.116	1182.938	1180.527	0.48	1.00409	0.00014	0.00010
5	Flight spare	1178.165	1182.911	1180.538	0.47	1.00403	0.00007	0.00003
6	Flight spare	1178.193	1182.833	1180.513	0.48	1.00394	−0.00002	−0.00006
7	Flight	1178.097	1182.873	1180.485	0.49	1.00405	0.00010	0.00006
8	Flight spare	1178.290	1182.905	1180.598	0.49	1.00392	−0.00004	−0.00008
	Specification	1178.28	1182.94	1180.6 +0.0, −6.0	<0.50	1.00395	±0.0001[a]	

[a]Allowable deviations for the alignment gratings are three times this value.

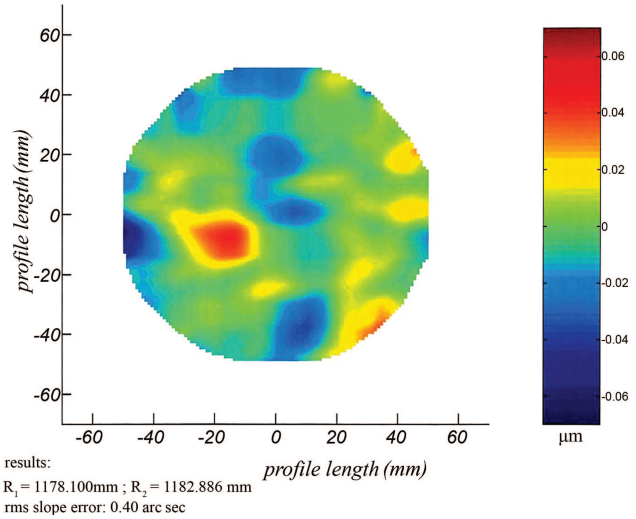

Fig. 2. Residual figure error in micrometers for toroidal grating 3.

duce high reflectivity in its wavelength band. These coatings achieved high reflectivity in the 170–210 Å and 250–290 Å bands with peak reflectances of 32% and 23% at wavelengths of 195 and 268 Å, respectively.[6] The telescope mirror is a superpolished off-axis parabola with a focal length of 1939 mm, a measured figure accuracy $<\lambda/47$ at 632 nm and a rms microroughness of <4 Å. The 160 mm diameter mirror was fabricated from Zerodur by Tinsley Laboratories, Inc.[7] and has a usable diameter of 150 mm. The flight grating (FG) is specified to be a toroid[8,9] with ideal radii of 1182.98 mm in the dispersion direction and 1178.28 mm in the perpendicular direction and with a figure slope error <0.5 arc sec rms. The grating microroughness was <0.25 nm rms. The gratings were fabricated by Carl Zeiss Laser Optics GmbH[10] from 100 mm diameter fused-silica blanks and have a usable area 90 mm in diameter.

A family of eight toroidal grating blanks was produced for this program, including the flight item, surrogate (alignment) gratings (AGs), and the necessary spares. To minimize deviations in the figure from grating to grating, the grating blanks were all polished in the same fabrication lot. Table 1 summarizes the data on the eight grating figures as measured by Zeiss. Grating 7 has been selected as the flight grating (FG). Grating 3 was selected as the corresponding AG. FG 7 has a toroidal radius of 1182.873 mm in the dispersion direction and 1178.097 mm in the perpendicular direction with a figure slope error of 0.49 arc sec rms and a microroughness of <0.25 nm rms. As with all Rowland-type mounts, the ratio of the radii ($R1/R2$) must be tightly controlled. Figure 2 shows the toroidal figure error for EIS grating 3.

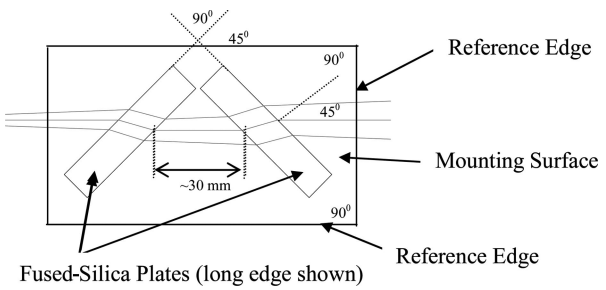

Fig. 3. Toroid test fixture. The fused-silica plates are 25 mm × 38 mm × 8.54 ± 0.1 mm thick, with surfaces parallel to <30 arc sec.

B. Null Tester for Toroid

To verify the figure and orientation of the toroidal grating, a null tester was constructed to evaluate the grating at the center of curvature.[11] Two plane-parallel fused-silica plates were chosen to provide aberration correction for the test fixture. The plates were tilted +45° and −45° with respect to the axis (90° with respect to one another) and were aligned so that the 90° angle formed between the two plates is in the plane of Fig. 3. The symmetrical two-plate arrangement does not disperse or deviate the beam. The fixture is used in double pass (both the input and the reflected beams pass through the plates) with the input point source 5.0 mm off axis in the out-of-plane direction such that source and its image are separated by 10 mm in the out-of-plane direction. For ease of alignment the tilted plate assembly was bonded to two fused-silica side plates into a box structure and has two reference surfaces, one parallel to and one perpendicular to the axis of the toroid. The tilted plates were 8.54 mm thick and flat to <1 wavelength at 6328 Å. All angles were within 3 arc min. This fixture was used with a 20 µm pinhole as a light source, and a circular 20 µm return image was observed without any noticeable comatic flares or aberrations.

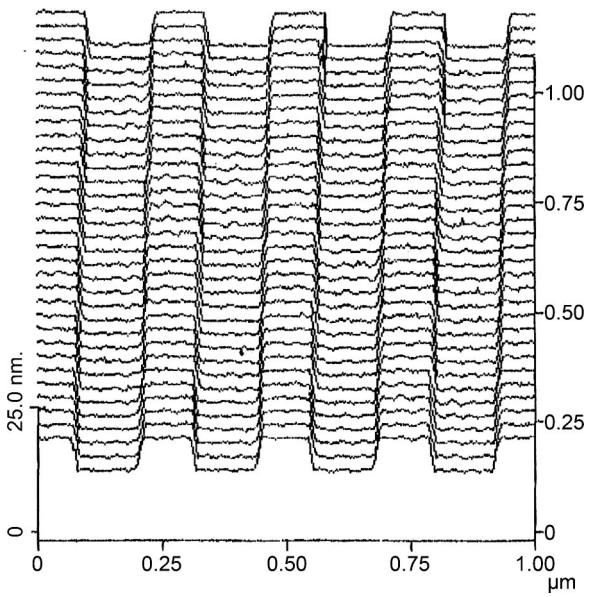

Fig. 4. AFM profile of grating grooves in a 1 µm × 1 µm region near grating center on an EIS laminar grating. The mean groove depth is 6.4 nm and the land width is 108 nm in this case.

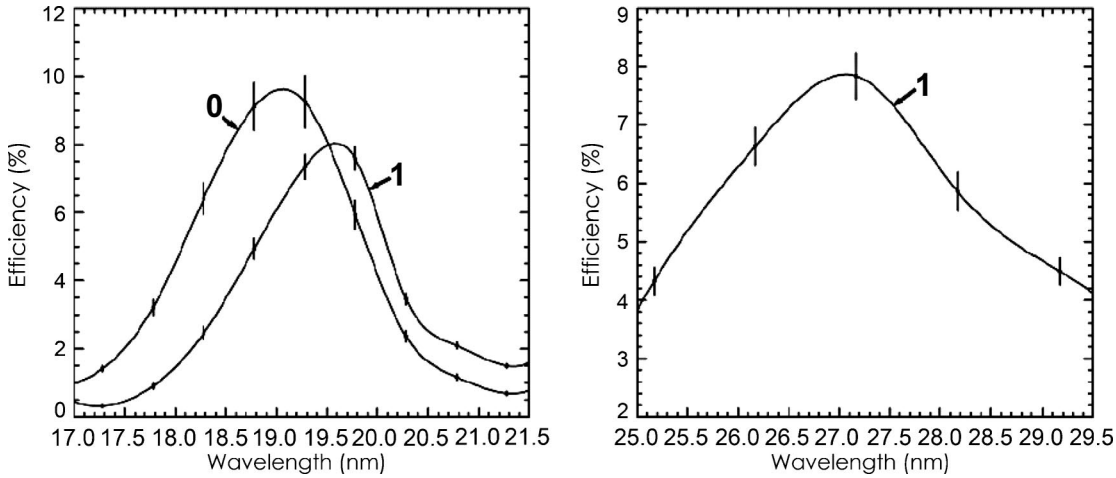

Fig. 5. Multilayer-coated grating efficiency in the short- and long-wavelength EIS bands.

C. Grating Groove Pattern

The grating pattern was holographically recorded and subsequently ion etched into a fused-silica blank. A single uniform laminar groove pattern having a frequency of 4200 lines/mm, a groove depth of 6.0 nm, and a 0.8:1 land-to-groove ratio was chosen to provide nearly equal diffraction efficiencies in the two EIS spectral bands. This grating configuration, when illuminated near normal incidence, maximizes the diffraction efficiency in the first order while minimizing the efficiencies in other orders.[3,12] The grating chosen for flight has a groove depth of 6.7 nm. Figure 4 shows the results of an atomic force microscope (AFM) measurement of the groove profile of an EIS laminar grating. The multilayer-coated grating efficiencies for the zero and first orders are shown in Fig. 5. The peak efficiencies are 8.0% at 196 Å in the short-wavelength band and 7.9% at 271 Å in the long-wavelength band.

D. Surrogate Grating Approach

Aligning and focusing a high-resolution EUV grating presents two special problems: (1) all EUV focusing must be done in vacuum with windowless light sources, and (2) the high-density ruling precludes using visible light diffraction. To overcome these difficulties, the following approach was developed. A surrogate or alignment grating was produced identical to the 4200 line/mm FGs except for the ruling density. The two gratings were mounted in mechanically identical holders with a common kinematic base and locating pins.

To facilitate spectrograph alignment, the gratings were fabricated with several optical fiducials. The gratings were specified to have the rear surface polished flat and normal to the optical axis to within 1 arc min and to have four facets (one every 90°) on the margin, parallel or perpendicular to the groove direction to within 1 arc min. The AG was also fabricated with the same fiducials. The AG had essentially the same figure as the FG, but with the two D-shaped sectors ruled with 146 and 208 lines/mm, respectively. This ruling density placed an image of the 546 nm Hg emission line in the center of each EIS detector. The AG was used to align and focus the EIS spectrograph at 546 nm in air; the resulting mechanical and optical geometry was then transferred to the EUV gratings using the

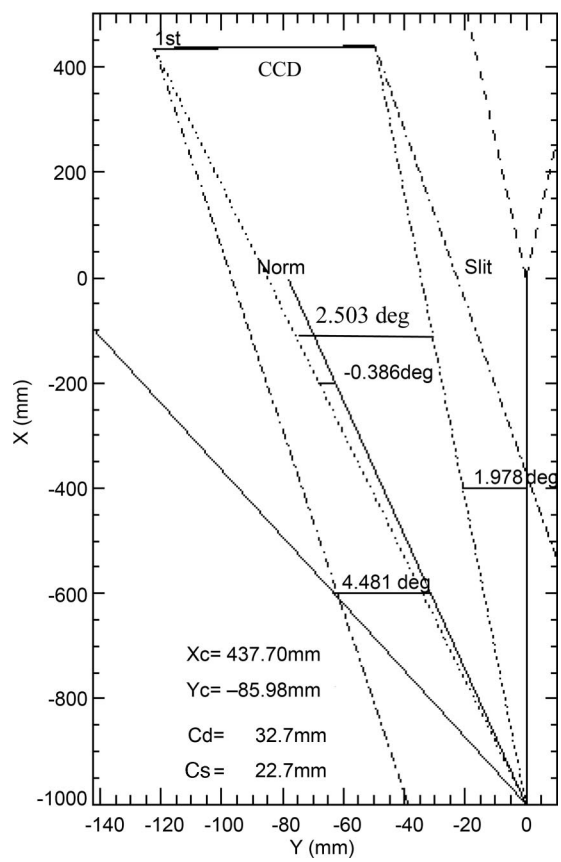

Fig. 6. Optimized configuration of the toroidal grating spectrometer. The center of the grating is at (−1000,0). The Y scale is greatly expanded in this figure relative to the X scale. The dashed vee converging at the slit represents the volume occupied by the light path from the telescope mirror.

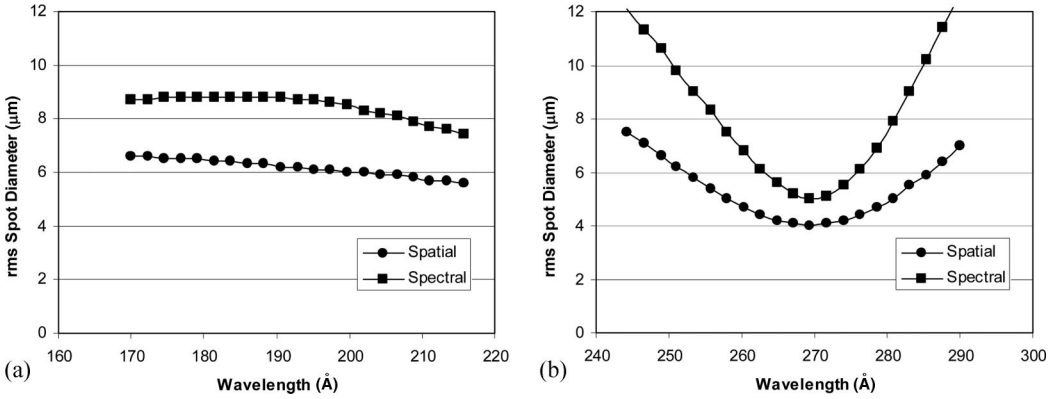

Fig. 7. Grating spot size diameter for a point at the center of the slit as a function of wavelength (a) for the short-wavelength band and (b) for the long-wavelength band. These spot dimensions are for the grating only and should be added in quadrature to the spot sizes of the off-axis parabola telescope mirror to estimate the spot sizes for the full EIS instrument. The spatial dimension is north–south on the solar disk and the spectral dimension is east–west.

fiducials. This intermediate step greatly simplified the spectrograph alignment and successfully minimized vacuum operations.

E. Spectrometer Optimization

The grating mount geometry was optimized using a ray-trace program. The grating ruling frequency was chosen to be 4200 lines/mm, the maximum ruling density easily accommodated by Zeiss's holographic recording equipment. The general constraints included an overall instrument length of ~3 m, a required plate scale of 1 arc sec/pixel, and 13.5 μm CCD pixels. Within these limitations, the ray-trace code optimized the grating parameters to provide the smallest averaged rms spot size over the spectral bands 170–210 Å and 250–290 Å and over a spatial field of view of ±250 arc sec. The optimization calculation used separate D-shaped portions of the grating for each wavelength range but was constrained to an identically figured and singly ruled optic for both ranges. This calculation produced a different optical prescription and smaller spot sizes when compared with prescriptions optimized using the full grating aperture for both wavelength ranges.

Figure 6 shows the final optimized configuration of the toroidal grating spectrometer. A slit to grating center distance of 1.000 m and a grating center to CCD distance of 1.440 m gave a 1.44 net magnification. The final plate scale is the desired 1 arc sec/pixel. The dispersion for the optimized spectrometer at the CCD is 1.65 Å/mm or 0.0223 Å/pixel. The optimization yielded a configuration with both the incidence angle and the diffraction angle near normal. The angle of incidence at the center of the grating is 4.481° and the diffraction angles for the wavelength bands of interest range from −0.386° to 2.503°. Representative plots of the spot diameters (double the rms blur) with wavelength and along the slit are given in Figs. 7 and 8. The spot size error budget is included in Table 2.

F. Telescope Mirror Mechanism

The articulated primary mirror produces a high-quality solar image at the spectrograph entrance slit. The predicted imaging performance is described in Table 3. The mirror mechanism (MIR) provides two different types of articulation for moving the solar image perpendicular to the slit length. A piezoelectric

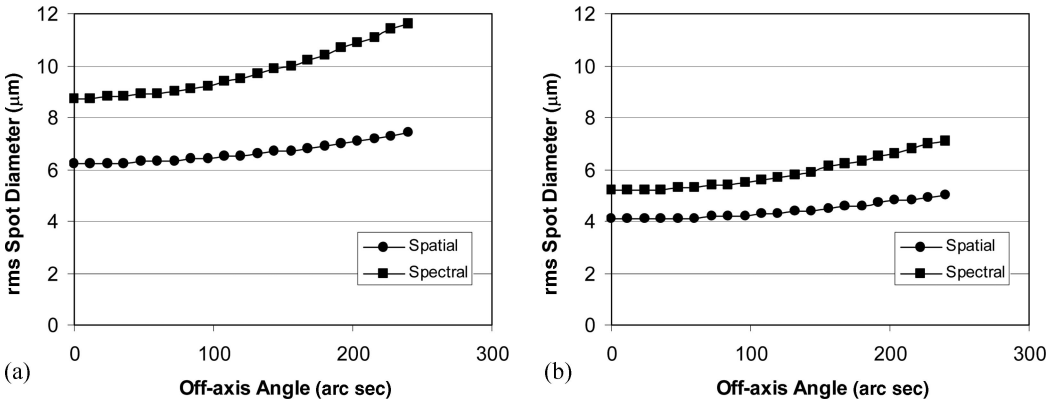

Fig. 8. Grating spot size diameter along the slit at the central wavelength of each detector (a) for the short-wavelength band (193 Å) and (b) for the long-wavelength band (267 Å). Position 0 is the slit center and the off-axis angle is measured north or south along the slit. See caption to Fig. 7.

Table 2. Predicted EIS Grating Imaging Performance

Contributing Error	Applicable Tolerance	Equivalent Spot Diameter (μm)[a]	Comments
Grating slope deviation	0.49 arc sec rms	13.7	Figure error measured
Optical aberrations		<13.5	Calculated with ray trace
Radii tolerance $R1/R2$	0.0001	10.9	Figure error measured
Alignment error budget		<5	Individual parts tolerance and error budget developed
Focus error budget		13.5	Allowed despace
		Total 26.4	Root sum square
Instrument spectral width with 1 arc sec slit		29.6	Root sum square
Instrument spectral width 2 arc sec slit		37.8	Root sum square

[a]Equivalent spot diameters are given at the CCD focal plane. The diameters correspond to twice the rms radius.

transducer (PZT) actuator and flex pivot arrangement provides a tilt motion. The mirror tilt range is >300 arc sec; the equivalent image motion at the slit is >600 arc sec. The measured reproducibility of the mirror for relatively large movements is better than 2 arc sec over 30 min in a laboratory environment. Nominal rastering operations will be conducted with the PZT. Linear motion is provided by a conventional ball screw and linear bearing arrangement. The linear step size is equivalent to 0.30 arc sec on the solar surface with a total range greater than ± 2750 steps or ± 825 arc sec. On orbit, the linear motion will be used primarily to repoint the instrument field of view.

The essential components of the MIR mechanism are shown in Fig. 9. The mirror central hub is bonded onto a bracket with flexible epoxy. As a weight reduction measure, the rear surface of the mirror was pocketed to remove ~50% of the total mass from the blank. The bracket is mounted by two flexible pivots to the linear moving stage of the mechanism. The combined load-bearing capacity for the two flex pivots is >4000 N. The flex pivots have high radial and axial stiffness, all-metallic construction, nearly infinite life for low-amplitude motion, are stiction free, and are inherently frictionless. They also have a wide operating temperature range. A 60 μm nominal extension PZT actuator with a flexible tip is used to provide the necessary rotary motion. The tip of the PZT is mounted to an arm rigidly coupled to the mirror mounting bracket. An Invar bracket is used to secure the low-voltage PZT actuator structure to the linear moving stage of the MIR mechanism. The Invar bracket closely matches the net coefficient of thermal expansion of the PZT material and support structure and reduces the angular drift of the mechanism with temperature. Strain gauges integral to the PZT are used to sense the PZT extension and remove the substantial hysteresis. The PZT strain gauge is implemented in a Wheatstone bridge with ~1400 Ω of resistance in each branch. Since the signal levels are relatively low (<10 μV digital steps), the bridge resistors and bridge output amplifier circuitry are mounted on a small card integral with the MIR mechanism. The preload on the PZT is ~700 N, which is sufficient for the application. The open- and closed-loop performance is shown in Fig. 10. The reproducibility of the PZT in a laboratory environment is shown in Fig. 11.

As shown in Fig. 9, the linear moving stage is attached to the fixed stage with three linear, self-aligning bearings mounted on hardened steel shafts. The linear bearings are mounted with flexures to the moving stage to minimize alignment difficulties. The match and fit of the linear bearings to the hardened steel rods were accomplished using tight tolerance machining as well as final machining adjustments on the various mechanical parts. The bearings consist of a cage (outer sleeve and ball retainer) of black Delrin, bearing plates of 8260 heat-treated steel, and balls of grade 25 chrome steel. The linear bearings provide self-alignment in all directions, which reduces sensitivity to machining tolerances. The bearings are of space-grade material and were disassembled for precision cleaning. The linear scan drive consists of a 30°

Table 3. Predicted EIS Mirror Imaging Performance

Contributing Error	Applicable Tolerance	Equivalent Spot Diameter (μm)[a]	Comments
Optical aberrations		<13.5	Modeled geometric and diffraction effects
Electronic noise in the PZT		<7.75	Measured
Focus error budget	<150 μm along the optical axis	<11.1	Sensitivity of focus test arrangement
		Total 19.12	Root sum square

[a]Equivalent spot diameters are given at the CCD focal plane. The diameters correspond to twice the rms radius.

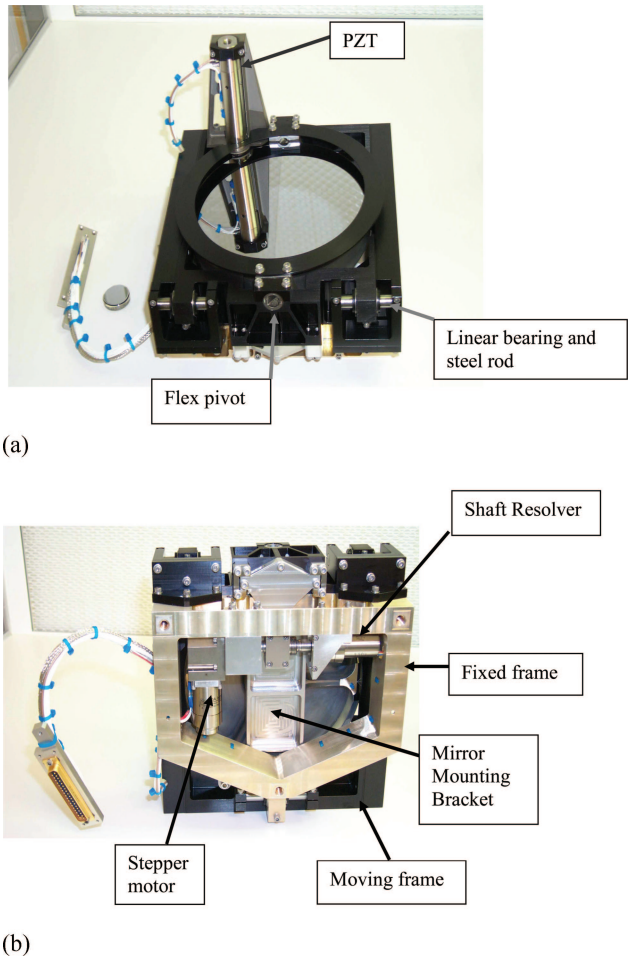

Fig. 9. Assembled flight MIR assembly: (a) front view and (b) rear view.

stepper motor with a 96:1 gearbox followed by a linear ball screw actuator with a 0.049 cm pitch and is identical to the grating focus mechanism actuator (see below). Backdriving is prevented with a passive brake on the back shaft of the motor rated for loads >1000 N. The ball screw backlash is <13 μm of motion. The load-bearing capacity of the thrust bearings is sufficient (>4000 N) for this application. The position of the linear stage is sensed with a rotary resolver directly mounted to the end of the ball screw. A small gearbox incorporated into the resolver allows each linear position to be associated with a unique resolver angle. As shown in Fig. 12, the residual errors are periodic in nature with a maximum amplitude of ±15 μm or 1.6 arc sec on the solar surface.

G. Clamshell and Aluminum Filters

During the 1970s, NRL in collaboration with G. Steele of Luxel Corporation developed large-format thin aluminum filters for the EUV instruments on Skylab.[13] High-purity vapor-deposited aluminum (VDA) foils between 1000 and 1500 Å thick pass EUV wavelengths between 170 and 650 Å while blocking the visible, infrared, and near-UV wavelengths.[14] We have implemented a front filter array (FFA) of four Al

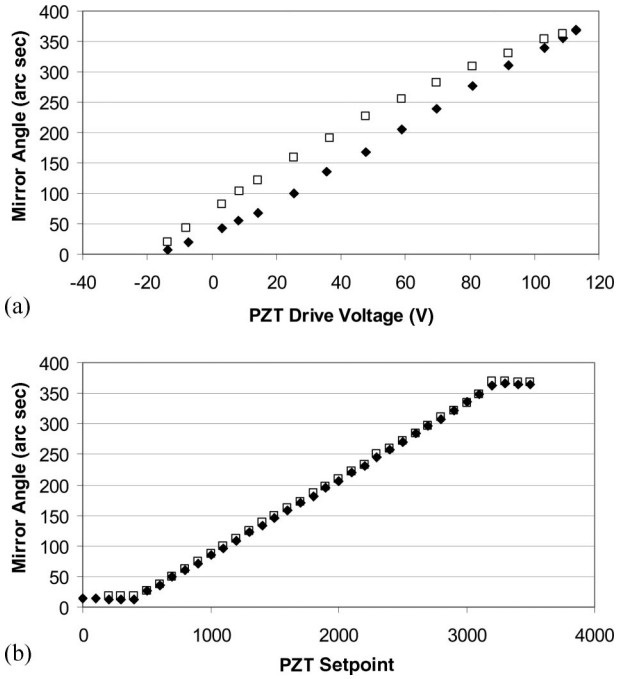

Fig. 10. Performance of the PZT actuator during (a) open loop (voltage control) and (b) during closed loop (digital number control) with feedback. The solid symbols are for increasing actuator voltage and the open symbols are for decreasing voltage. The working setpoint range is between 600 and 3200.

filters to cover the EIS front aperture to reject heat and visible light, and a second small Al spectrometer extrance filter (SEF) behind the spectrometer slit to reject any out-of-band light that could leak through any pinholes that might develop in the front filter. For a rocket launch, these thin foils must be protected from the severe environment of vibrations, acoustics, and debris and from oxidation and contamination. A special chamber is provided for launching the four EIS FFA filters under vacuum (Fig. 13). It is a short cylinder having front and rear doors hinged to open in the vacuum of space much like a clam and is named the Clamshell (CLM) assembly.

The CLM has an oval internal cross section of ~190 mm × 210 mm and a depth of ~50 mm. The

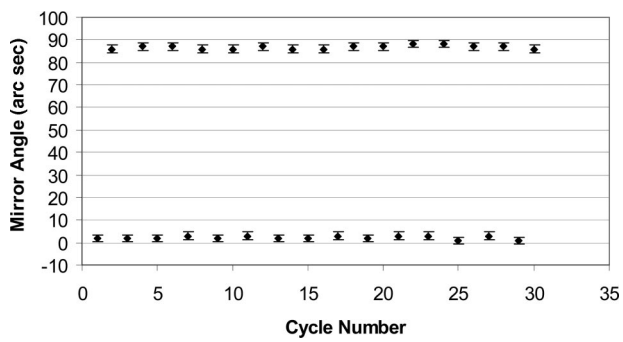

Fig. 11. Measured reproducibility of the PZT actuated mirror in a laboratory environment. In this test, the mirror was repeatedly commanded between two positions ~85 arc sec apart. The error bars correspond to the ±1.5 arc sec measurement accuracy.

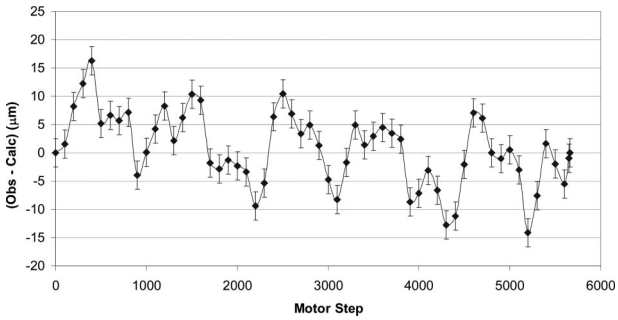

Fig. 12. Measured deviation of the MIR linear displacement as a function of motor step number. The error bars correspond to the limits of the measurement micrometer accuracy.

two doors are ~200 mm × 220 mm ovals and are sealed with Viton O-rings. Two high-output paraffin actuators with redundant heaters operate separate latches for the front and rear doors. A torsion spring actuates the opening of each door, assisted by two stiff spring plungers to initiate separation of the O-ring seal. The CLM is evacuated through a 6.3 mm stainless-steel valve sealed with a Kel-F plunger. The CLM is a lightweight (2.5 kg) Al structure built using high-vacuum design principles. It can be evacuated to $<10^{-4}$ Torr, and when properly conditioned will remain below 5 Torr for more than three months without pumping. It is equipped with two pressure sensors, one connected to the ground support equipment and one to the instrument housekeeping and telemetry via the mechanism and heater controller electronics. To reduce acoustic loads on the filter, EIS will be launched with CLM pressures below 5 Torr. An engineering model CLM assembly passed through vibration and acoustic testing at NRL with a flight design filter in place. The pressure during these tests was 7.5–10 Torr.

The CLM and filter arrangement is evolved from similar items used on the Transition Region and Coronal Explorer (TRACE) mission,[15] with the front aperture divided into four quadrants, each with its own filter (see Fig. 14). The filters are supported on a nickel mesh of 40 μm wires on 390 μm centers. The meshes were specially designed for EIS and electroformed by Stork Veco Inc.[16] and are 18 μm thick. The chief failure mode for filters under vibration test was found to be metal fatigue in the mesh at the point where the wires joined the filter frame. During the Skylab[12] mission, this problem was solved by adding a fillet of soft Epon material around the margin of each filter to reduce the stress concentration there. To reduce the possibility of contamination, we wanted to eliminate the Epon, so we modified the support mesh. Each mesh is pie shaped with a margin of solid Ni 5 mm wide on the outside shaped to match the filter frame. This margin is glued to the filter frame and the solid margin material extends 1 mm into the filter area. Fillets of 0.025 mm radius were formed at each intersection of the wires with the margin. Figure

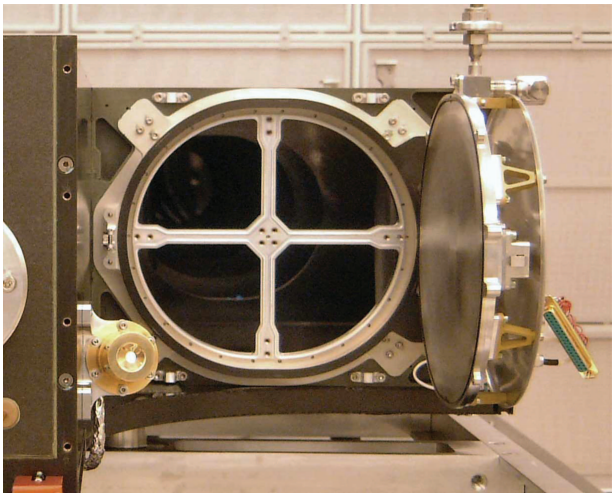

Fig. 14. EIS front filter CLM assembly with doors open. The support spider for four filter quadrants is shown without the Al filters.

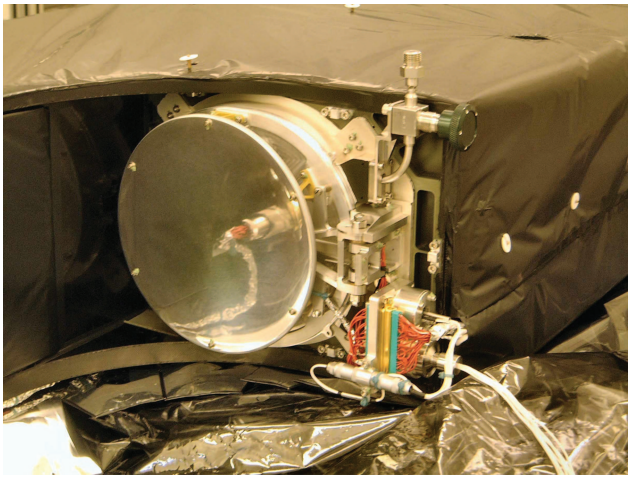

Fig. 13. EIS Clamshell assembly mounted on the instrument. The evacuation port is at the top and a thin thermally coated polished metal disk on the front reflects incoming solar heat. The instrument itself is covered with black thermal blanketing material.

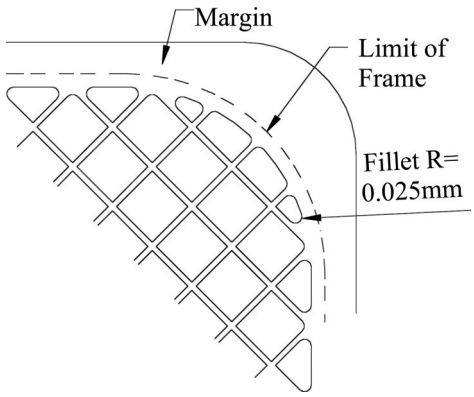

Fig. 15. Schematic (not to scale) showing detail of the filter margining method for the EIS. The wires are 40 μm wide on 390 μm centers. The gap between the support frame and the open filter area is 1 mm. Where possible, the mesh wires join the frame at a 45° angle.

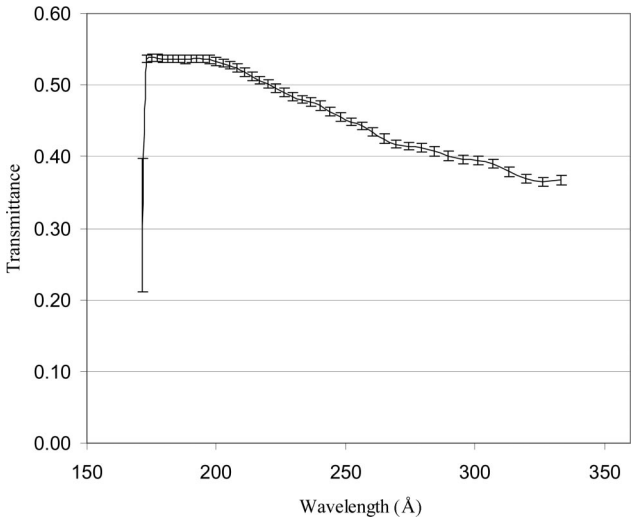

Fig. 16. Average transmission for an EIS Al filter 1500 Å thick. The data are from 24 scans at points on a 15 mm grid arranged over the filter surface. The error bars are 1 standard deviation. These data are for the mounted filters and include the ~20% loss due to the mesh. The step at 170 Å is the Al L-edge. Additional Si and Al filters were used in the beamline to eliminate the small amount of second-order light from the monochromator in the 170–300 Å range of interest.

15 is a schematic of the filter mesh modification. This margining method, with the solid material extending into the open filter area, reduced the calculated stress levels in the mesh by a factor of 10. Each mesh has an open area equal to 80% of the total. The meshes with attached foils were glued to Al frames for installation in the CLM. Each frame had a blackened tongue-and-groove light seal around its margin to allow air pressure to equalize on both sides of the filter.

The EUV transmission of each filter was measured with synchrotron radiation at the X24C Beamline at the National Synchrotron Light Source, Brookhaven National Laboratory. The synchrotron beam passed through a monochromator and sampled an ~2 mm diameter spot on the filter. Each filter was measured at a grid of points on 15 mm spacing. Figure 16 is a summary plot of the transmission of a typical filter, in this case 1500 Å thick. Table 4 is a summary of the measured thicknesses and transmission properties of the EIS filters produced.

Another filter property measured was the visible light rejection. This was done by mounting the filter on a lighttight box and illuminating it with diffuse white light. The rear surface of the filter was imaged onto a CCD and the transmitted light was measured. The visible transmission fraction was $\leq 8.3 \times 10^{-7}$ for all filters. The filters are an important part of the

Table 5. Measured Thermal Radiative Properties EIS Filter Material[a]

Sample Information	α	ε_n
Sun-facing surface VDA on Ni mesh	0.07	0.02
	0.08	0.02
	0.07	0.02
Non-Sun-facing surface (with Ni mesh)	0.22	0.05
	0.23	0.06
	0.22	0.06

[a]These measurements were performed by Swales Aerospace Contamination and Thermal Coatings Group, 13 March 2002, TCR 0004-011502, EIS Project 2109-011.

Table 4. Foil Thickness and Transmission Properties of EIS EUV Filters

Filter	Serial Number, Foil Number	Thickness (Å)	Visible Transmission[a]	Transmission at 270 Å (%)	Transmission at 195 Å (%)
SEF 3608C	052, 9730-1	1516	3.17×10^{-9}	36.3	49.2
	053, 9717-1	1476	1.16×10^{-8}	36.1	48.8
	054, 9730-1	1516	3.17×10^{-9}	36.3	49.0
	055, 9730-1[b]	1516	3.17×10^{-9}	35.9	48.1
	057, 9717-1	1476	1.16×10^{-8}	36.3	48.6
	058, 9730-1	1516	3.17×10^{-9}	36.1	48.8
FFA 3551C	017, 9849-1	1555	19×10^{-8}	27.8	43.9
	011, 9900-1	1582	2.46×10^{-8}	34.7	47.3
	013, 9730-2[b]	1516	1.90×10^{-8}	36.6	49.3
	015, 9863-2	1513	2.53×10^{-8}	34.3	46.5
	010, 9738-2[b]	1500	7.40×10^{-9}	35.4	48.4
	016, 9738-1	1500	7.40×10^{-9}	37.1	49.2
FFA 3552C	011, 9846-1[c]	1580	1.80×10^{-8}	28.3	44.7
	017, 9747-2	1476	2.57×10^{-8}	40.4	51.6
	018, 9664-1	1446	4.01×10^{-8}	38.3	50.0
	013, 9792-2[b]	1650	2.57×10^{-8}	36.3	49.0
	014, 9770-1[b]	1476	1.27×10^{-8}	41.7	53.7
	016, 9792-1	1650	1.69×10^{-8}	41.0	56.2

[a]As reported by vendor.
[b]Selected flight item.
[c]Spoiled.

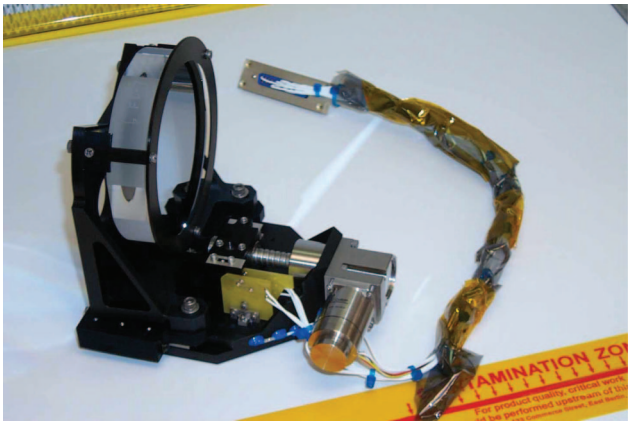

Fig. 17. Grating FL 7 in its flight mounting. Two of the four polished facets on the margin of the grating blank are visible. The motor, gearhead, and ball screw compose the focus mechanism. Two small circuit boards hold LEDs and photodiodes for the limit sensors.

thermal balance system of the instrument, rejecting most of the incident solar radiation. The solar absorbance α was measured according to the American Society for Testing and Materials (ASTM) E903-82 standard test method and the emittance ε_n was measured in the 5–40 μm band by the ASTM E408-71 standard test method (see Table 5).

H. Grating Focus Mechanism

Figure 17 is a photograph of the EIS grating mounted in the focusing mechanism. Two of the four fiducial facets can be seen in the photograph on the edge of the grating blank. The rear surface of the grating is bonded to the mounting bracket at the grating center with a space-grade flexible epoxy. The grating surface figure was checked before and after bonding. This bonding procedure did not introduce any measurable optical figure distortion. The grating and bracket subassembly are on a moving stage mounted to the mechanism baseplate with a pair of crossed roller bearing slides. These compact precision bearings allow the linear motion of large loads with high accuracy and repeatability, low friction, and low starting force. The rails selected for the focus mechanism have a combined load capacity of 450 N in all directions. Each bearing consists of a pair of hardened steel ways containing 90° V grooves and a row of alternatively crossed cylindrical rollers. The hardened steel rollers are captive in a brass cage for easy handling, assembly, and permanent alignment.

The translation stage is driven by a geared stepper motor and ball screw combination. The actuator consists of a 30° stepper motor with a 96:1 gearbox followed by a linear ball screw with a 3.175 mm pitch. Each motor step results in a 2.8 μm displacement of the grating. Backdriving is prevented by a passive brake on the back of the motor shaft rated for loads >1000 N. The ball screw backlash is <13 μm. The load-bearing capacity of the thrust bearings are sufficient (>4000 N) for this application. The mechanism is aligned to drive the translation stage along the slit–grating axis. The focus mechanism incorporates a set of three optical encoders (light-emitting

Table 6. EIS Slit Width Summary[a]

Nominal Width (arc sec)	Serial Number	Measured Width (μm)	Measured Width (arc sec)
1	101C	9.5	1.01
2	102A	19.0	2.02
40	103A	384	40.9
266	104D	2506	266.6

[a]Measured dimensions are ±0.5 μm for the 1 and 2 arc sec slits and ±2 μm for the 40 and 266 arc sec slits.

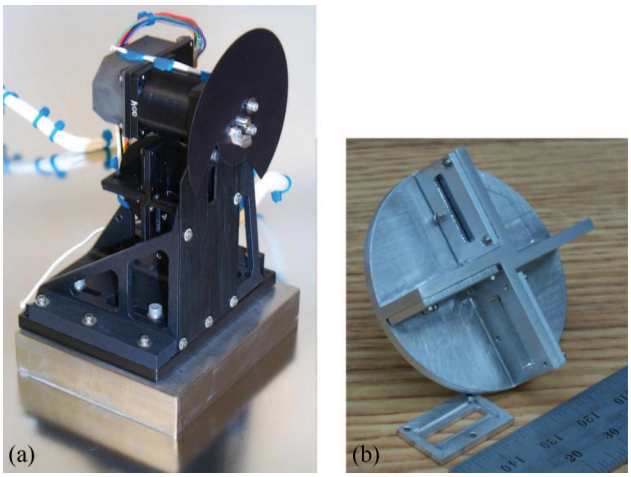

Fig. 18. a) Slit–slot mechanism assembly. The four slits are on a paddle wheel and are exchanged by 90° rotations of the wheel. The shutter blade and motor are also attached to this assembly. b). Paddle wheel and slit frame before blackening.

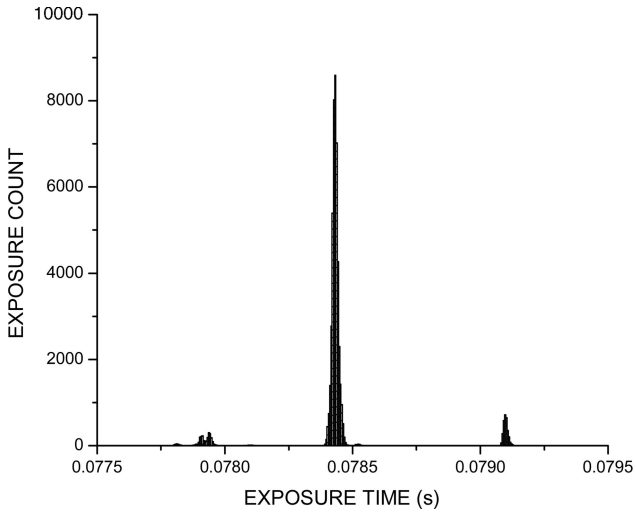

Fig. 19. Histogram of recorded exposure time for 49,936 exposures taken on 9 June 2002 with the development model shutter. These test exposures were taken as part of mechanism life testing. The exposure times are within 1 ms of the nominal value. The trimodal distribution is an artifact of the ~1 ms granularity of the software timing used to control shutter exposure times.

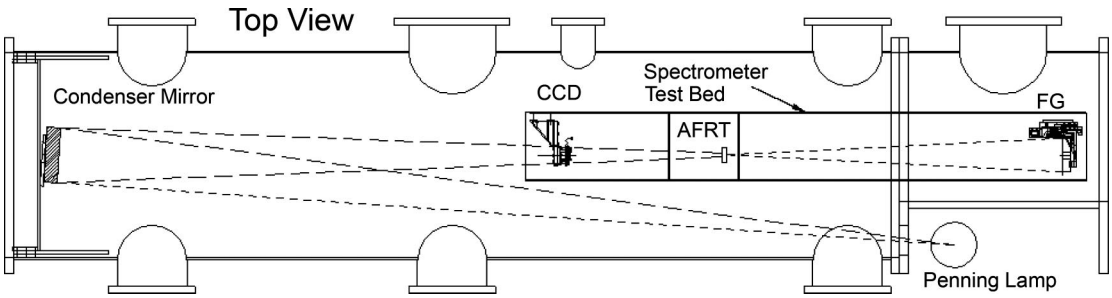

Fig. 20. EIS grating optical test facility.

diode–photodiode combination) to indicate the positive and negative travel limits and a central position.

I. Slit–Slot Exchange and Shutter Assembly

The EIS instrument incorporates a combined slit–slot interchange and shutter mechanism shown in Fig. 18a). On the slit–slot exchange mechanism, each slit was bonded onto an Al frame using a flexible epoxy. The frame was then bolted to a paddle wheel as shown in Fig. 18b). Tight fabrication tolerances on the frame and paddle wheel controlled the placement of the slits. The paddle wheel mount is directly attached to the output shaft of a rotary actuator. The axis of rotation is perpendicular to the chief optical ray. The actuator consists of a 30° stepper motor attached to a gearbox with a 1:108 mechanical advantage with an integral resolver. There are 324 steps between 90° paddle wheel positions. A rotary resolver is coupled to the output shaft with antibacklash gearing. The rotary actuator reproducibly replaces each of the spectrometer slits to <2 μm perpendicular to the optical axis and <10 μm along the optical axis focus direction. This precision preserves both wavelength calibration and instrument focus for each slit. Final performance testing of the mechanism showed that these requirements were achieved. In addition, the mechanism was found to drive reproducibly from either direction with backlash <10 μm motion at the center of the slit along the optical axis. The resolver has an accuracy of <15 arc min, sufficient to discriminate between individual motor steps.

The instrument slits and slots were fabricated from a Si substrate by the NASA Goddard Space Flight Center photolithography group. The material for the slit was a two-side polished <100> plane Si wafer, 75 μm thick and 50.7 mm in diameter. A thick Si oxide was grown on the wafers and used as the etch mask for anisotropic etching of the <100> plane Si from the slit area, while the <110> planes acted as the etch stop and provided a 54° bevel to the slit edges. The mask was printed on the wafer using standard techniques that remove oxide in the region to be etched. The bare Si on the slit area was then etched away. Once the slit is opened up, oxide was removed from the rest of the wafer, forming the frame around the slit. Precise metrology was carried out to determine the slit width. Results are shown in Table 6.

The shutter mechanical design is based on a similar mechanism constructed for the Lockheed Soft X-ray Imager.[17] The shutter is driven by a brushless dc motor. The necessary drive phase communication is provided by an optical encoder assembly mounted to the shaft of the motor. The motor was specifically designed to provide the high speed and high torque for precise control of rotating assemblies required by this application. During laboratory testing, the shutter and associated flight drive electronics successfully obtained a series of 78 ms exposure with $<5\%$ photometric error. Figure 19 shows the measured timing precision for nearly 50,000 shutter cycles.

3. Extreme-Ultraviolet Imaging Test of the Spectrometer Gratings

A. Stand-Alone Grating Tests

The EUV imaging properties of the toroidal grating were measured in a stand-alone laboratory test and then again at the instrument level of assembly. For the laboratory test, a spectrometer test bed was built. Figure 20 is a schematic of the laboratory test setup. The test bed is mounted with a U.S. Air Force 1951 resolution target (AFRT) at the slit position, a 1500 Å thick Al EUV filter from Luxel[18] just behind the slit,

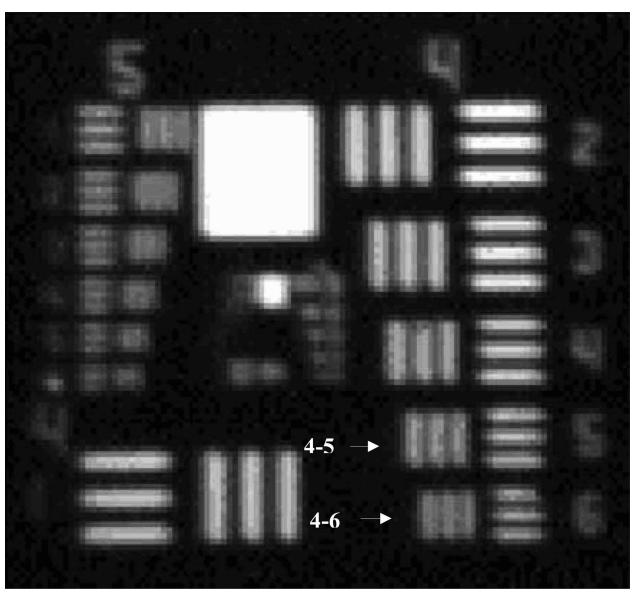

Fig. 21. Magnified AFRT image recorded using He II 256 Å line radiation. The arrows indicate the direction of the scans in Fig. 23.

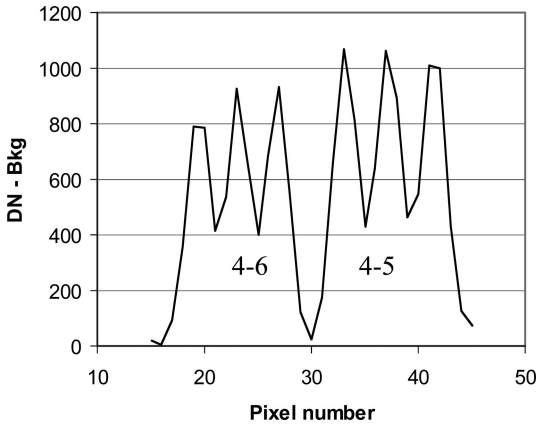

Fig. 22. Column plot through the horizontal bars of groups 4-5 and 4-6 in Fig. 21. DN, corresponding data number.

a kinematic grating base, the toroidal grating, and an engineering model CCD detector.[19] This test bed was placed on an optical rail in a clean high-vacuum chamber that was customized for the EUV imaging test. The chamber was fitted with a Penning discharge lamp[20] that was operated with Mg cathodes and He or Ne gas depending on the wavelength band of interest. Resolution measurements were made in the short-wavelength band of the grating using the Mg III, IV lines at 171, 180, 182, and 187 Å. In separate trials, resolution measurements were made in the long-wavelength band using the He II line at 256 Å and the Ne III lines at 251, 267, and 283 Å. When using He and Ne to produce long-band spectra, the lamp was operated at a pressure of $\sim 5 \times 10^{-4}$ Torr with a current of 200 mA and a voltage of ~600 V. The short-band spectra were produced by operating the lamp at a current of ~500 mA and a voltage of ~1.5 kV. As shown in Fig. 20, a 150 mm diameter dual multilayer-coated spherical mirror (condenser) with a radius of curvature of 2235 mm was used to image the lamp onto the AFRT in the spectrometer box. The two multilayer coatings on this mirror were matched to those of the grating.

The AG was first placed in the spectrometer test bed and adjusted to produce a sharp image in the EIS long-wavelength band in the 546 nm Hg spectral line. A PenRay Hg lamp[21] was used to backilluminate the AFRT. Using two kinematic grating holders with a common base, the alignment grating orientation and focus were transferred to the EUV grating. Autocollimating theodolites were used to view the grating side facets and rear surface, and a microscope was focused on the front surface to locate the grating focus position. Having completed the alignment orientation transfer with visible light, the 4200 lines/mm FG was placed into the spectrometer test bed and the Al filter was installed for vacuum EUV testing. The system was then evacuated and the Penning discharge lamp was used for EUV illumination. The grating focus motor was used to translate the FG along the incident optical axis to achieve the best focus at EUV wavelengths.

A cryogenically cooled e2v CCD with an active area of 1024 pixels × 2048 pixels was used to record the EUV images. Typical exposure times were ~1 min for He II and Ne III lines and ~2 min for the Mg III, IV lines. During vacuum EUV testing, no shutter was used. Environmental vibrations were found to have a significant impact on the quality of the images being recorded. To achieve the required resolution, it was necessary to float the optical table on pneumatic legs, temporarily turn off all nearby clean room fans, and to isolate the turbobacking pump from the vacuum chamber.

Figure 21 displays a magnified image of the central region of the AFRT, which was recorded with the He II 256 Å line radiation. Using the 0.106 arc sec/μm telescope scale factor, the 2 arc sec or two-pixel Nyquist limit in the focal plane corresponds to 18.8 μm at the slit in the FG object plane. On the AFRT, group 4-5 has a 19.7 μm line width (2.09 arc sec resolution) and 4-6 has a 17.5 μm line width (1.87 arc sec resolution) spanning the Nyquist limit. Pixel intensity modulation can be seen in the groups 4-5 and 4-6 with limiting resolution near 5-5 and 5-6. Figure 22 shows a plot through the horizontal bars of groups 4-5 and 4-6 after background subtraction from the image. Figure 23 shows a row plot through the vertical bars of groups 4-5 and 4-6. The vertical bars in the AFRT were parallel to the floor and thus suffered more from building vibration than did the hor-

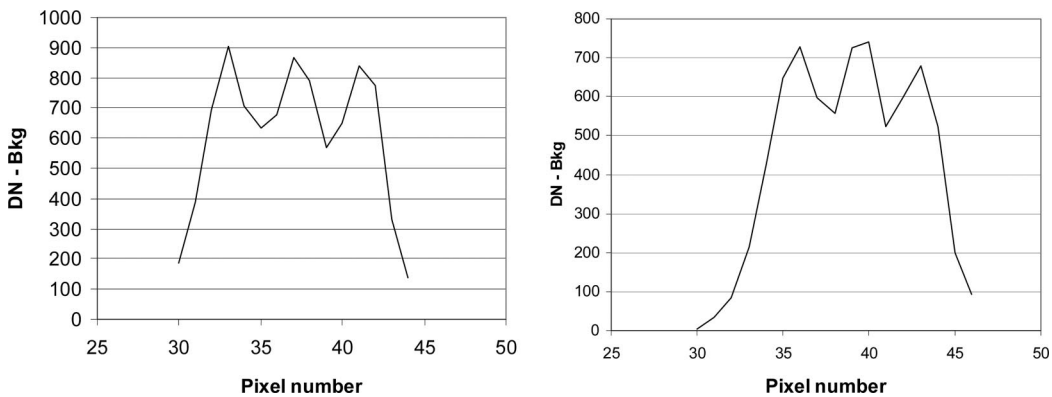

Fig. 23. Row plot through the vertical bars of groups 4-5 and 4-6 in Fig. 21. DN, corresponding data number.

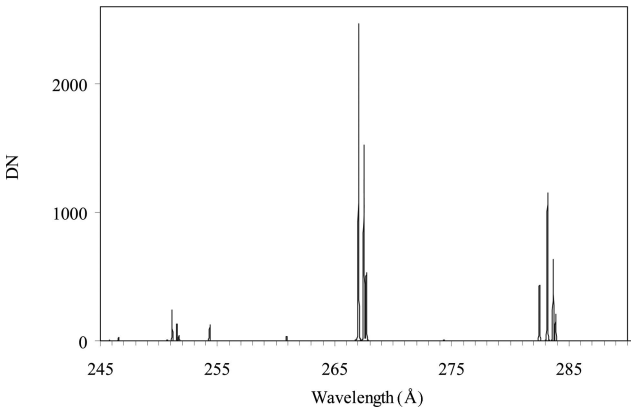

Fig. 24. Ne and Mg Penning discharge spectrum in the long-wavelength band recorded with the EIS spectrograph. DN, corresponding data number.

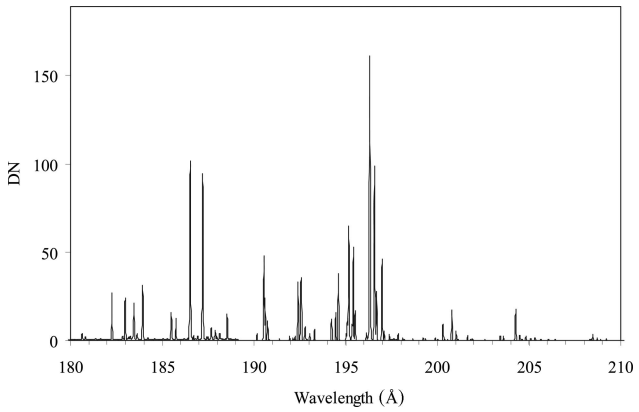

Fig. 26. Representative short-wavelength Ne and Mg spectra recorded with the EIS instrument. DN, corresponding data number.

izontal bars. The short-band imaging test yielded a similar performance to that observed in the long band but required much longer exposures.

B. Integrated Instrument Tests

When all acceptance testing was completed at the NRL, the grating, slit, filter, and mirror assemblies were shipped to the Rutherford Appleton Laboratory in the UK. There, the instrument was fully assembled and aligned in its flight configuration. Tests with two EUV light sources were performed. First, a 150 mm diameter spherical mirror was used to collimate the radiation from the Penning discharge source and fill the EIS telescope aperture to achieve optimal focusing. The lamp was again operated with He or Ne gas and Mg cathodes. Representative spectra recorded with a 9.5 μm slit are shown in Figs. 24 and 25 for the long-wavelength band using Ne. Figures 26 and 27 show representative spectra from the short-wavelength band from ionized Mg and Ne. Figure 28 shows a He 256 Å line profile and a Gaussian fit to the line profile. The FWHM He linewidth is 0.056 Å (2.5) pixels for a measured spectrograph resolving power of 4571. Analysis of numerous line images on a row-by-row basis showed that spectral lines from the 1 and 2 arc sec slits were tilted by less than one pixel top to bottom over 200 pixel-long line images in both CCDs. Many of the spectral lines observed are found in the National Institute of Standards and Technology database[22] and in Kelly's compilation,[23] but a number of new lines of Ne II, III, and IV were identified in the course of this work.[24–26]

The second source was a Physicalisch-Technische Bundensanstalt calibrated Al hollow-cathode lamp and Wolter telescope. This light source is calibrated against a synchrotron source and has relative standard uncertainties of ±8% in well-calibrated lines.[27] The hollow-cathode light is run backwards through a Wolter grazing-incidence telescope to produce a collimated beam 5 mm in diameter. This beam is stepped across the telescope aperture to calibrate EIS at a large number of points. The image of the aperture of the hollow cathode is ~60 arc sec in diameter at the focus of the telescope mirror, so the entire beam can enter the spectrometer through the 266 arc sec slot. Collecting the entire beam in this way and imaging it onto the CCDs allows for the end-to-end

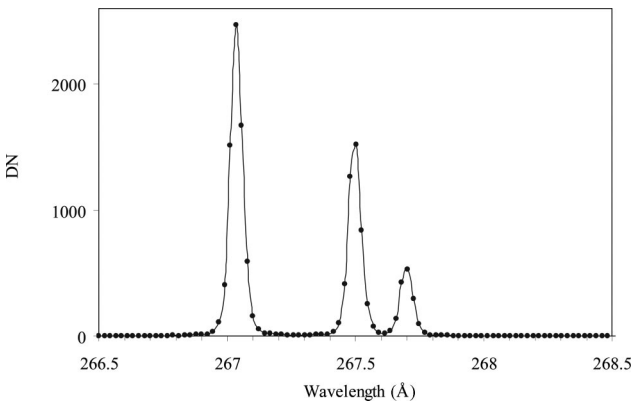

Fig. 25. Detail of the $2s^22p^4$-$2s^22p^33s$ Ne III lines at 267.051, 267.070, 267.498, 267.510, 267.529, and 267.709 Å as observed in the long-wavelength detector of EIS. The source was the collimated beam from the Ne and Mg Penning discharge. The FWHM of the fitted line profile is 0.0577 Å (2.59 pixels). DN, corresponding data number.

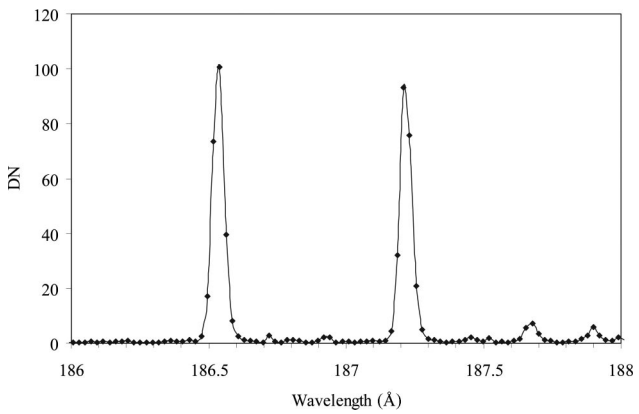

Fig. 27. Mg III lines at 186.5149 and 187.1977 Å in the short-wavelength band. The fitted FWHM of both lines is 0.047 Å (2.12 pixels). DN, corresponding data number.

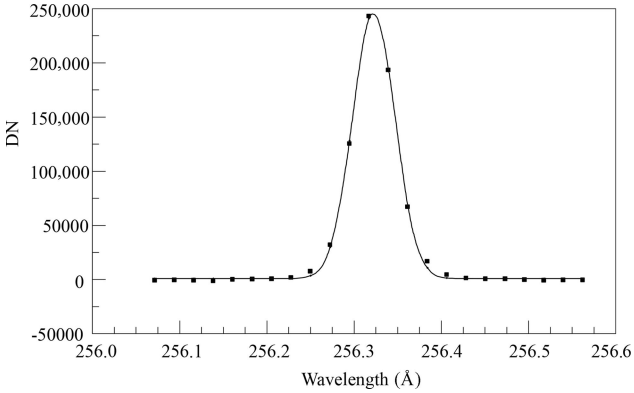

Fig. 28. He II 256 Å line from a Penning discharge as observed by EIS. The solid curve is a Gaussian function fitted to the CCD data number (DN).

calibration of the EIS sensitivity.[28] The radiometric calibration of EIS is described by Lang *et al*.[29]

4. Summary

This paper describes the design and measured laboratory performance of the optics and mechanisms for the EIS instrument. The measured performance of the instrument is consistent with the objective of obtaining high-quality rastered EUV spectral images of the solar atmosphere. Precision rotary and linear motions of the primary mirror are available to raster and repoint the solar image, respectively. A slit–slot exchange assembly uses a unique design to place accurately one of the four selectable slits at the telescope focal plane. The focus of the grating spectrograph is adjustable in fine increments. The shutter is capable of 100 ms exposures with a reproducibility of $<5\%$. The instrument was designed for optimal performance while maintaining achievable alignment and fabrication tolerances. Final end-to-end laboratory tests of EUV image quality are consistent with the final spot diagrams and predicted error budget. Laboratory measurements show that the EIS spectrograph is capable of observing spectra with a resolving power of 4571 in the EUV. With Nyquist-limited resolution, very high spectral resolving power and the high efficiency of a two-optical-element telescope and spectrograph, the EIS grating spectrograph will be a powerful tool to observe the plasma dynamics of the solar atmosphere.

The EIS instrument was built by an international consortium lead by the Mullard Space Science Laboratory (MSSL). The authors thank J. L. Culhane of MSSL, EIS instrument principal investigator; George Doschek, NRL, principal investigator to NASA; and T. Watanabe, National Astronomical Observatory of Japan, Japanese principal investigator, for their constant support and encouragement. In addition, we thank NASA Marshall Space Flight Center's Solar-B program manager, Larry Hill, for his support and guidance during the development, testing, and integration of the EIS instrument.

We gratefully acknowledge the technical contributions of many individuals on the EIS international team. We particularly acknowledge the contributions of the following individuals to the successful development and test of the EIS optics and mechanisms: Khalid Al-Janabi, Mark Anderson, Jerry Batterton, Giles Case, Chris Castelli, Rahil Chaudery, Therese Errigo, Tim Gordon, Joe Hammerbacher, Bob Haynes, Don Lilley, Barry Kent, Clive Longstaff, Fred Lund, Saad Mahmoud, Layne Marlin, Brian Martini, Forbes Powell, David Rippington, David Roberts, Don Robertson, Kathy Seymour, Robert Sullivan, Clay Sylvester, Carrie Townsend, Andrew Uhl, Randy Waymire, Graham Willis, and Matthew Whillock.

Support for the EIS construction program is provided by the Particle Physics and Astronomy Research Council (UK), NASA, and the Ministry of Education and Culture (Japan). Work at the NRL and NASA Goddard Space Flight Center was supported by the NASA Marshall Space Flight Center funded part of the EIS Solar-B program.

Note added in proof. The Solar-B satellite was launched on 22 September 2006 and has been named Hinode.

References and Notes

1. C. Korendyke, C. M. Brown, J. Seely, and S. Meyers, "International collaboration yields a high-performance EUV spectrometer for the Solar-B spacecraft," OE Mag. **2,** 23–26 (2002).
2. J. L. Culhane, C. M. Korendyke, T. Watanabe, and G. Doschek, "Extreme-ultraviolet imaging spectrometer designed for the Japanese Solar-B satellite," in *Instrumentation for UV/EUV Astronomy and Solar Missions,* S. Fineschi, C. M. Korendyke, O. H. Sigmund, and B. E. Woodgate, eds., Proc. SPIE **4139,** 294–312 (2000).
3. T. Harada, S. Moriyama, and T. Kita, "Mechanically ruled stigmatic concave grating," Jpn. J. Appl. Phys. **14,** Suppl. 14-1, 175–179 (1975).
4. T. Harada and T. Kita, "Mechanically ruled aberration-corrected concave gratings," Appl. Opt. **19,** 3987–3993 (1980).
5. T. Harada, H. Sakuma, K. Takahashi, T. Watanabe, H. Hara, and T. Kita, "Design of a high-resolution extreme-ultraviolet imaging spectrometer with aberration-corrected concave gratings," Appl. Opt. **37,** 6803–6810 (1998).
6. J. F. Seely, C. M. Brown, D. L. Windt, S. Donguy, and B. Kjornattanawanich, "Normal-incidence efficiencies of multilayer-coated laminar gratings for the Extreme-Ultraviolet Imaging Spectrometer (EIS) on the Solar-B mission," Appl. Opt. **43,** 1463–1471 (2004).
7. Tinsley Laboratories, Inc., 4040 Lakeside Dr., Richmond, Calif. 94806-1963.
8. H. G. Beutler, "The theory of the concave grating," J. Opt. Soc. Am. **35,** 311–350 (1945).
9. H. Haber, "The torus grating," J. Opt. Soc. Am. **40,** 153–165 (1950).
10. Carl Zeiss Laser Optics GmbH, 22 Carl Zeiss Strasse, 73447 Oberkochen, Germany.
11. J. Harlander, St. Cloud State University, St. Cloud, Minn. (personal communication, 2001).
12. M. P. Kowalski, T. W. Barbee, Jr., K. F. Heidemann, H. Gursky, J. C. Rife, W. R. Hunter, G. G. Fritz, and R. G. Cruddace, "Efficiency calibration of the first multilayer-coated holographic ion-etched flight grating for a sounding rocket high-resolution spectrometer," Appl. Opt. **38,** 6487–6493 (1999).

13. R. J. Schumacher and W. R. Hunter, "Thin aluminum filters for use on the Apollo Telescope Mount XUV spectrographs," Appl. Opt. **16,** 904–908 (1977).
14. F. Powell, "Care and feeding of soft x-ray and extreme ultraviolet filters," in Laser-Induced Damage in Optical Materials, H. E. Bennett, L. L. Chase, A. H. Guenther, B. Newman, and M. J. Soileau, eds., Proc. SPIE **1848,** 503–514 (1992).
15. P. Chiemets, Smithsonian Astrophysical Observatory, (personal communication, 1999).
16. Stork Veco B. V., P.O. Box 10, 6960 AA Eerbeek, The Netherlands.
17. D. Akin, Lockheed Martin Advanced Technology Center, Palo Alto Calif. (personal communication, 2000).
18. Luxel Corp., P.O. Box 1879 Friday Harbor, Wash. 98250.
19. e2v Technologies, 106 Waterhouse Lane, Chelmsford, Essex CM1 2QU, UK.
20. D. Finley, S. Bowyer, F. Paresce, and R. Malina, "Continuous discharge Penning source with emission lines between 50 Å and 300 Å," Appl. Opt. **18,** 649–654 (1979).
21. UVP, Inc., 2066 W. 11th St., Upland, Calif. 91786.
22. National Institute of Standards and Technology, "NIST Atomic Spectral Database," http://physics.nist.gov/PhysRefData/ASD/index.html (2005).
23. R. L. Kelly, "Atomic and ionic spectrum lines below 2000 angstroms: hydrogen through krypton. part I (H-Cr)," J. Chem. Phys. Ref. Data **16,** Suppl. 1, 1–649 (1987).
24. A. E. Kramida, C. M. Brown, U. Feldman, and J. Reader, "Extended EUV and UV spectrum of Ne II," Phys. Scr. **74,** 156–167 (2006).
25. C. M. Brown (Space Science Division, U.S. Naval Research Laboratory, 4555 Overlook Avenue, S.W., Washington, D.C. 20375), A. E. Kramida, U. Feldman, and J. Reader, are preparing a manuscript to be called "Extended EUV spectrum of Ne III."
26. A. E. Kramida, C. M. Brown (Space Science Division, U.S. Naval Research Laboratory, 4555 Overlook Avenue, S.W., Washington, D.C. 20375), U. Feldman, and J. Reader, are preparing a manuscript to be called "Extended EUV spectrum of Ne IV."
27. J. Hollandt, M. Kühne, and B. Wende, "High-current hollow cathode source as a radiant intensity standard in the 40–125 nm wavelength range," Appl. Opt. **33,** 68–74 (1994).
28. J. Lang, B. J. Kent, and J. F. Seely, "The proposed calibration of Solar B EIS," in *Radiometric Calibration of SOHO,* ISSI Scientific Rep. SR-0002, A. Pauluhn, M. C. E. Huber, and R. von Steiger, eds. (European Space Agency, 2002), pp. 337–345.
29. J. Lang, B. J. Kent, W. Paustian, C. M. Brown, C. Keyser, M. R. Anderson, G. C. R. Case, R. A. Chaudry, A. M. James, C. M. Korendyke, C. D. Pike, B. J. Probyn, D. J. Rippington, J. F. Seely, J. A. Tandy, and M. C. R. Whillock, "Laboratory calibration of the Extreme-Ultraviolet Imaging Spectrometer for the Solar-B satellite," Appl. Opt. **45,** 8689–8705 (2006).